Original Article

Appreciable biosafety, biocompatibility and osteogenic capability of 3D printed nonstoichiometric wollastonite scaffolds favorable for clinical translation

Yingming Wei [a], Zhongxiu Wang [a], Lihong Lei [a], Jiayin Han [a], Shuaiqi Zhong [a], Xianyan Yang [b], Zhongru Gou [b,**], Lili Chen [a,*]

[a] *Department of Oral Medicine, The Second Affiliated Hospital, School of Medicine, Zhejiang University Hangzhou, 310008, China*
[b] *Bio-nanomaterials and Regenerative Medicine Research Division, Zhejiang-California International Nanosystem Institute, Zhejiang University, Hangzhou, 310058, China*

A B S T R A C T

Background: Alveolar bone destruction due to periodontal disease often requires a bone graft substitute to reconstruct the anatomical structures and biological functions of the bone tissue. Despite significant advances in the development of foreign ion-doped nonstoichiometric wollastonite bioceramics ($CaSiO_3$, nCSi) for alveolar bone regeneration over the past decade, the in vivo biosafety and osteogenesis of nCSi scaffolds remain uncertain. In this study, we developed a customized porous nCSi scaffold to investigate the in vivo biocompatibility and osteogenic properties of nCSi bioceramics.
Methods: Six percent Mg-doped nCSi bioceramic scaffolds were fabricated by digital light processing (DLP), and the scaffold morphology, pore architecture, compressive strength, in vitro biodegradation, and apatite-forming ability of the bioceramic scaffolds were investigated systematically. Subsequently, an alveolar bone defect rabbit model was used to evaluate the biocompatibility and osteogenic efficacy of the nCSi bioceramics. Animal weight, hematological test, blood biochemical test, wet weight of the main organs, and pathological examination of the main organs were conducted. Micro-CT and histological staining were performed to analyze the osteogenic potential of the personalized bioceramic scaffolds.
Results: The nCSi scaffolds exhibited appreciable initial compressive strength (>30 MPa) and mild mechanical decay over time during in vitro biodissolution. In addition, the scaffolds induced apatite remineralization in SBF. Bioceramic scaffolds have been proven to have good biocompatibility in vivo after implantation into the alveolar bone defect of rabbits. No significant effects on the hematological indices, blood biochemical parameters, organ wet weight, or organ histopathology were detected from 3 to 180 days postoperatively. The porous scaffolds exhibited strong bone regeneration capability in the alveolar bone defect model of rabbits. Micro-CT and histological examination showed effective maintenance of bone morphology in the bioceramic scaffold group; however, depressed bone tissue was observed in the control group.
Conclusions: Our results suggest that personalized nCSi bioceramic scaffolds can be fabricated using the DLP technique. These newly developed strong bioceramic scaffolds exhibit good biocompatibility and osteogenic capability in vivo and have excellent potential as next-generation oral implants.
The translational potential of this article: Tissue-engineered strategies for alveolar bone repair require a bone graft substitute with appreciable biocompatibility and osteogenic capability. This article provides a systematic investigation of the in vivo biosafety and osteogenic property of nCSi to further development of a silicate-based bioceramics materials for clinical applications.

* Corresponding author. Department of Oral Medicine, the Second Affiliated Hospital, School of Medicine of Zhejiang University, Jiefang Road 88#, Hangzhou, 310009, China.
** Corresponding author. Zhejiang-California International Nanosystems Institute, Zhejiang University, Hangzhou, 310058, China.
  E-mail addresses: zhrgou@zju.edu.cn (Z. Gou), chenlili_1030@zju.edu.cn (L. Chen).

1. Introduction

Periodontal disease is a typical chronic inflammatory response characterized by the destruction of the gingiva, alveolar bone, periodontal ligament, and cementum, leading to various periodontal defects [1,2]. Beube first employed boiled cow bone powder in periodontal defects in 1947 and reported successful results, including pocket eradication, mobility elimination, and new bone formation [3]. Recently, several investigators have reported the implantation of bone grafts and substitutes for the treatment of bone defects caused by periodontal disease. In the past three decades, Ca phosphate and Ca silicate bioceramics have received significant attention for periodontal bone regeneration because of their appreciable biosafety, mechanical stability, and biodegradability [4].

Wollastonite ($CaSiO_3$, CSi) is one of the simplest silicate-based bioceramics with a high bioactivity that facilitates bone regeneration. Calcium and silicon ions released from CSi can induce vascularization and bone healing in the defect area [5–7]. Xu et al. investigated the in vivo performance of CSi and β-tricalcium phosphate (β-$Ca_3(PO_4)_2$, β-TCP) ceramics in a rabbit calvarial defect model. The micro-CT and histomorphometric analysis confirmed that the degradation rate of CSi was much higher than that of β-TCP, and more newly formed bone was observed with CSi in the early stage [8]. Owing to their excellent biocompatibility and osteoconductivity, CSi bioceramics have been widely used for orthopedic applications [9,10]. Although CSi bioceramics have been widely studied for orthopedic applications, in vitro evaluations by Wang et al. [11] and Ni et al. [12] showed that the overly high biodegradation rate of pure CSi may be unfavorable for the proliferation and differentiation of osteoblasts in the scaffolds. Additionally, owing to their inherent poor sintering and brittle nature, pure CSi scaffolds are substantially suboptimal for the repair of bone defects because of insufficient mechanical support [13,14].

Based on the above concerns, Xie et al. investigated the effect of Mg-substituted Ca in CSi on the physicochemical and mechanical properties of nonstoichiometric wollastonite (nCSi) through a chemical coprecipitation method [15]. It is abnormal but expected that, when below 10 mol% Ca was substituted by Mg, the crystalline phase of wollastonite was retained on nCSi, accompanied by outstanding compressive strength and fracture toughness (3.2–3.6 MPa $m^{1/2}$). The Mg dilute doping strategy is highly effective for improving the mechanical parameters and biodegradation rate of nCSi ceramic scaffolds in vitro and in vivo [16]. More recently, Shao et al. [17] used a direct ink writing technique to fabricate the porous nCSi scaffolds and implanted in the rabbit alveolar bone defect model to evaluate their stimulatory effect on bone tissue regeneration in comparison with β-TCP scaffolds. Their results revealed that nCSi scaffolds with 10% Mg substitution (CSi–Mg10) exhibited moderate biodissolution and appreciable osteogenic capability within 4 months. Most recently, studies have also confirmed that nCSi scaffolds with 6% Mg substitution (CSi–Mg6) can effectively achieve bone tissue regeneration in craniomaxillofacial defects, such as orbital, mandibular, or alveolar bone defects [18–21].

Although an increasing number of studies have focused on tuning the physicochemical properties of Ca-silicate bioceramic scaffolds to improve bone-repair performance, few studies have investigated the in vivo biosafety and biocompatibility of such silicate-based bioceramics. Yuan et al. reported the biocompatibility of a polyetheretherketone/CSi/porous tantalum cage in a goat model [22]. Unfortunately, the in vivo biosafety and biocompatibility of nCSi bioceramic scaffolds have not yet been reported. As the physicochemical, mechanical, and biodegradation properties of nCSi bioceramics are quite different from those of pure CSi, the biosafety of this new bioceramic for clinical applications should be evaluated systematically. Based on the aforementioned concerns, this study aimed to investigate the biocompatibility and efficacy of nCSi scaffolds in rabbits and lay the foundation for biosafety assessments and clinical translation. It is believed that the elucidation of the in vivo biosafety of silicate bioceramics with specific chemical and physical characteristics and an understanding of the osteogenic capability of 3D printed nonstoichiometric wollastonite scaffolds may ultimately result in the success of designing silicate-based bioceramic materials for clinical applications and predicting the outcomes of tissue regeneration in the future.

2. Materials and methods

2.1. Materials

The reagent-grade sodium metasilicate nonahydrate ($Na_2SiO_3\cdot9H_2O$), magnesium nitrate hexahydrate ($Mg(NO_3)_2\cdot6H2O$), calcium nitrate tetrahydrate ($Ca(NO_3)_2\cdot4H_2O$), and other inorganic reagents were purchased from Sinopharm Reagent Co., Ltd. The photosensitive resin for digital light processing (DLP) 3D printing was supplied by Ten Dimensions Technology Co (China).

2.2. Synthesis of nCSi powders

As described previously, Mg-substituted Ca nCSi ($Ca_{0.94}Mg_{0.06}SiO_3$) powders were synthesized by wet-chemical coprecipitation [15]. All the calcined powders were ground in an ethanol medium for 6 h by a planetary ball mill with a particle size of the resulting superfine powders below 5 μm. Inductively coupled plasma-optical emission spectrometry (ICP-OES; Thermo, UK) was used to determine the chemical composition of the nCSi powders. The phase composition of nCSi was verified using X-ray diffraction (XRD; Rigaku, Tokyo, Japan).

2.3. Preparation of nCSi scaffolds

The cylindrical porous scaffolds with a porosity of 55% and a pore dimension of Ø600 μm were designed by Solidworks software as described in our previous study [18]. The model of the nCSi scaffold was transformed into printing files and imported into the DLP facility supplied by 10 Dimensions Technology Co., China. Twenty grams of nCSi powder and 10 g of photosensitive resin were mixed using a mechanical agitator at a stirring speed of 1900–2000 r/min. After stirring for 30 min, the well-mixed slurry was poured into the slurry tank of the DLP printer. The slurry was solidified to a predetermined morphology and thickness and stacked into a definite structure under ultraviolet light. The exposure time for each layer was 3 s with a light intensity fixed to 10,000 μW/cm^2. After DLP printing, the scaffold samples were ultrasonically cleaned in deionized water and then dried for 12 h at 80 °C. Subsequently, the scaffold samples were sintered to reach a target temperature of 1150 °C for 2 h with a heating rate of 3 °C/min in a muffle furnace, followed by cooling naturally (Scheme 1).

2.4. Mechanical and bio-dissolution analysis in vitro

The compressive strengths of the nCSi scaffolds (n = 3) were measured using a static mechanical test machine (Instron 5566, Germany) at a cross-speed of 0.5 mm/min. To simulate the in vivo biodegradation of scaffolds, bioceramic samples (n = 9; 10 × 6 × 4 mm; m_0) were immersed in Tris buffer (initial pH: 7.4, temperature: 37 °C, liquid/solid ratio: 1.0 g/50 mL). After 1, 3, 5, 7, 14, and 21-days' immersion, 1 mL of the supernatant was collected for ICP-OES measurements (n = 3). Then, 1 mL of fresh buffer was added to the Tris buffer to maintain a constant solution volume. After 2-, 4-, and 6-weeks' immersion, the samples (n = 3) were extracted, rinsed by ethanol and dried at 80 °C overnight, followed by weighing (m_t). Mass loss was calculated as follows: remaining mass = $m_t/m_0 \times 100\%$. The compressive strengths of the immersed scaffolds were analyzed.

2.5. Surface re-mineralization in vitro

To evaluate the apatite-forming ability on the surface of porous
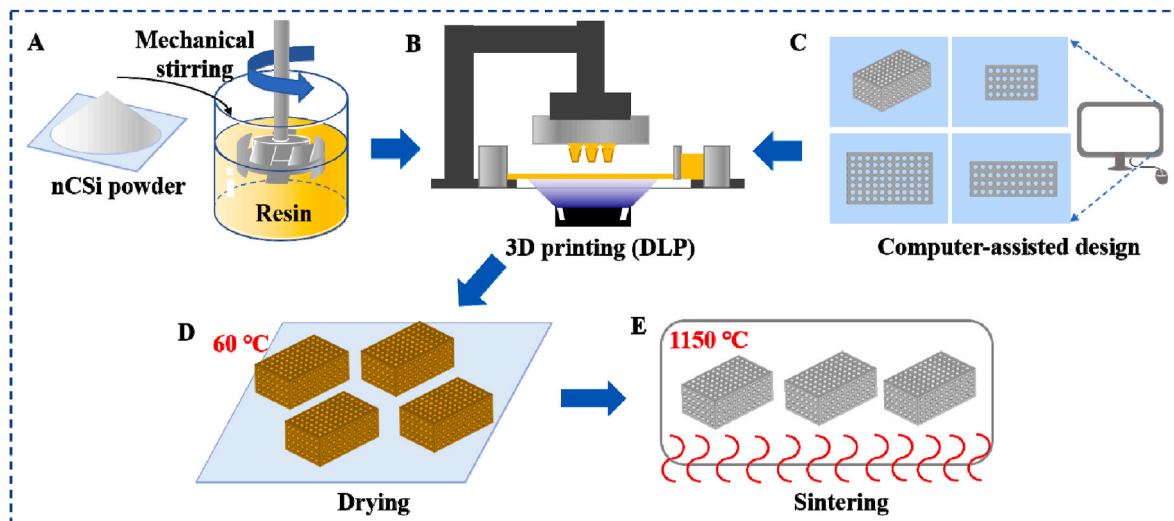
Scheme 1. Schematic of the 3D printing of nCSi bioceramic scaffolds. (A) The nCSi powder and resin were mixed to form a slurry. (B) Slurry was solidified using a DLP printer. (C) Porous scaffolds were designed using computer software. (D) Printed scaffolds were ultrasonically cleaned and dried. (E) The scaffolds were sintered to reach a target temperature of 1150 °C.

scaffolds, the nCSi sample (n = 6) was immersed in 10 mL simulated body fluid (SBF) at 37 °C. After soaking for 1 and 2 weeks, the scaffolds (n = 3) were washed, dried, and observed using a scanning electron microscope (SEM). Local chemical analysis was performed using energy-dispersive spectroscopy (EDX).

2.6. Biocompatibility and osteogenesis evaluation in vivo

2.6.1. Selection of experimental animals

Fifty male New Zealand white rabbits (2.5–3.0 kg) were purchased from Xinjian Rabbit Farm. The animals were kept in the ordinary laboratory of the Animal Experimental Research Center of Zhejiang Chinese Medical University (room temperature: 20–22 °C, relative humidity: 40%–60 %, 12 h/12 h alternating light and dark). All animal experiments and surgical procedures were approved by the Experimental Animal Management and Ethics Committee of the Zhejiang Chinese Medical University (IACUC-20210816-20). After adaptive feeding, all animals were weighed. Blood specimens were collected, and hematological and biochemical analyses were performed. Animals with abnormal hematological or blood biochemical parameters were excluded according to the reference intervals for New Zealand white rabbits [23,24]. Forty rabbits with normal weight, movement, mental
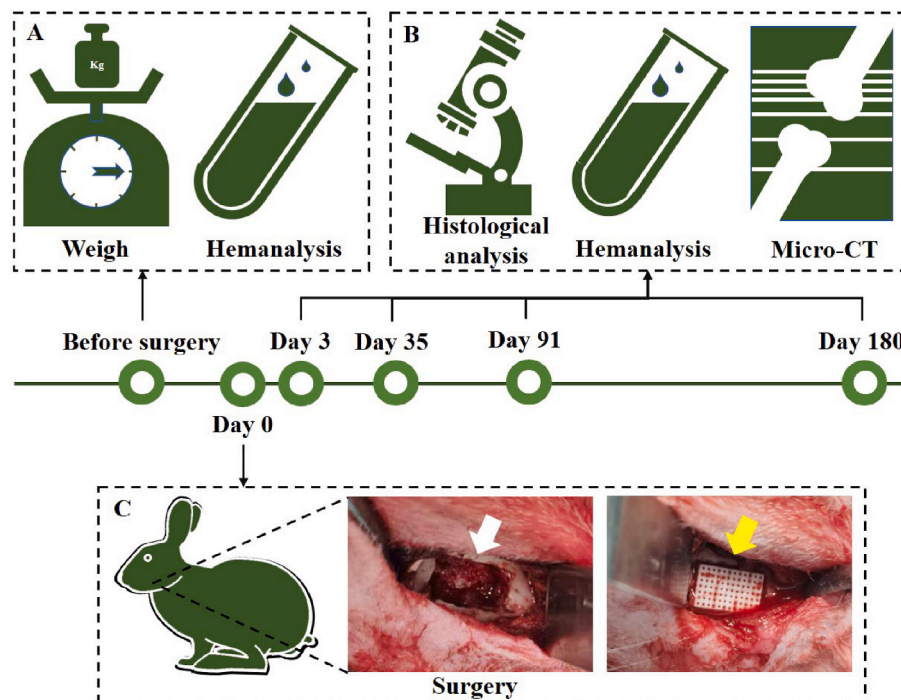
Scheme 2. Schematic of the evaluation of biocompatibility and osteogenic properties in vivo. (A) Animals were weighed, and blood samples were collected for hematological and blood biochemical analyses before surgery. (B) Hemanalysis was also performed 3, 35, 91, and 180 days after surgery. Histological analysis was conducted on the main apparatus, and the defect area was evaluated using micro-CT and histological analyses. (C) During surgery, bone defects (white arrow) were created on the mandible of the rabbit, followed by the implantation of bioceramic scaffolds (yellow arrow) (n = 5).

status, and hematological and blood biochemical parameters were randomly selected for the study. The animals were randomly divided into two groups (blank and nCSi groups), with 20 rabbits in each group. The experimental procedure is illustrated in Scheme 2.

2.6.2. Preparation of bone defect and implantation of bioceramic scaffolds

Before implantation, the sintered scaffolds were sterilized using an autoclave (121.3 °C, 20 min). General anesthesia was induced by isoflurane inhalation and maintained with 1% isoflurane. After the surgical region was shaved and disinfected, the skin was cut at the notch of the bilateral mandibular angle, and the subcutaneous tissue and muscle were bluntly separated, followed by elevation of the periosteum of the mandible. An alveolar bone defect (10 mm × 6 mm × 4 mm) was created using a high-speed fissure bur on the right mandible and rinsed with normal saline to cool it (Scheme 2C). The bioceramic scaffolds were then implanted into 20 defects in the nCSi group, and 20 defect cavities in the blank group were left empty. The left mandibles of all animals were sham-operated, and only the operation area was exposed; no defects were prepared. The periosteum, muscle, subcutaneous tissue, and skin were sutured layer-by-layer, and penicillin was applied locally before wound closure. After the operation, the animals were returned to rabbit cages in the feeding room, 800,000 units of penicillin were injected intramuscularly, and ibuprofen was administered orally for analgesia for 3 days. The rabbits were sacrificed after 3, 35, 91, and 180 days. The mandibles and other internal organs were harvested for further analysis.

2.6.3. General conditions of experimental animals

After surgery, the movement of the animals was not restricted, and the feeding method remained the same. The general condition of the animals, including their mental status, diet, activity, and wound recovery, was observed daily. The weights of the animals were recorded before the operation and 1 day, 3 days, and every week after surgery.

2.6.4. Haematological examination

Blood samples (1 mL) from five animals in each group were collected from the ear arteries to conduct hematological examinations at 3, 35, 91, and 180 days after surgery. White blood cell (WBC), neutrophil (NEUT), neutrophil percentage (NEUT%), lymphocyte (LYMPH), lymphocyte percentage (LYMPH%), monocyte (MONO), monocyte percentage (MONO%), eosinophils (EO), eosinophils percentage (EO%), basophilic granulocyte (BASO), basophilic granulocyte percentage (BASO%), red blood cell (RBC), hemoglobin (HGB), hematocrit (HCT), mean corpuscular volume (MCV), mean corpuscular hemoglobin (MCH), mean corpuscular hemoglobin concentration (MCHC), coefficient variation of red blood cell volume distribution width (RDW-CV), platelet (PLT), plateletcrit (PCT), mean platelet volume (MPV), platelet volume distribution width (PDW), platelet-larger cell ratio (P-LCR), reticulocyte (RET), reticulocyte percentage (RET%), reticulocyte hemoglobin (RET-He) were determined by the automatic hematological analyzer.

2.6.5. Biochemical examination

At 3, 35, 91, and 180 days postoperatively, 5 mL of blood was collected in plastic vacutainer tubes. After the blood samples were centrifuged at 3000 rpm for 10 min, biochemical indicators in serum, including alanine transaminase (ALT), aspartate aminotransferase (AST), total protein (TP), albumin (ALB), total bilirubin (TBIL), alkaline phosphatase (ALP), glucose (GLU), blood urea nitrogen (BUN), creatinine (CR), total cholesterol (TC), triglyceride (TG), creatine kinase (CK), chlorine, potassium, and sodium were photometrically measured by an automatic analyzer using a standard commercial kit.

2.6.6. Pathological analysis of the main apparatus

After the rabbits were sacrificed at 3, 35, 91, and 180 days, the hearts, livers, spleens, lungs, kidneys, brains, thymuses, testes, epididymides, and adrenal glands of the experimental animals were collected. The wet weights of the organs were recorded. Organs were fixed with 4% neutral formaldehyde, dehydrated, and embedded in paraffin. Hematoxylin/eosin (HE) staining was performed to evaluate the histopathological effects of nCSi bioceramic scaffold implantation on major organs.

2.6.7. µCT measurement

After harvesting, the mandibular specimens were observed to determine whether infection, fracture, loosening, or displacement of the scaffolds occurred in the surgical areas. Subsequently, the specimens were fixed in 4% neutral formaldehyde and measured by a microcomputer tomography system (µCT; Inveon µCT scanner, Siemens, Germany). The specimens were scanned to cover the entire defect region. The region of interest (ROI) was selected and 3D reconstructed virtually, the newly formed bone (NB) volume/total volume (BV/TV) ratio, scaffold residual volume/total volume (RV/TV), and trabecular number (Tb. N), and trabecular separation (Tb.Sp) was calculated.

2.6.8. Histological analysis

After CT analysis, the samples were rinsed with tap water and dehydrated with 70%, 80%, 95%, and 100% alcohol solutions, followed by embedding in polymethylmethacrylate. Then, the hardened specimens were cut into slices (200–300 µm) along the mesiodistal direction of defects with a saw microtone (SP1600, Leica, Germany). Finally, the original slices were ground, polished to reach a final thickness of 40–50 µm, and stained by HE and MacNeal's trichrome staining. The stained sections were observed and recorded using a light microscope (DMLA, Leica, Germany) at 10 × and 40 × magnifications.

2.7. Statistical analysis

All statistical analyses were performed using SPSS 19.0 (SPSS, Armonk, NY, USA). Mean value ± standard deviation (SD) was used for expressing quantitative data. Comparison of body weight, wet organ weight, hematological indicators, biochemical indicators, BV/TV, and Tb.N and Tb.Sp was analyzed using the Student's t-test. $P < 0.05$ was regarded as statistically significant.

3. Result

### 3.1. Phase composition of the bioceramic powders

ICP analysis showed that 6.67 mol% of Ca was substituted by Mg in nCSi; that is, the Mg content in the mass of this bioceramic powder was 1.39%. According to the XRD analysis, a low-temperature β phase of wollastonite remained as the crystalline phase of nCSi powder (Figure S1A; Supporting Information (SI)). Notably, with Mg doping in CSi, the (−2, −2, 2) crystal plane showed a slight peak shift to a higher 2θ value (from 29.91° to 30°/2θ) (Figure S1B; SI), indicating that Mg^{2+} (0.66 Å) replaced Ca^{2+} (1.00 Å) in the wollastonite lattice partially.

3.2. Primary characterization of the bioceramic scaffolds

After sintering at 1150 °C, the nCSi scaffolds displayed a dimension of 4.06 ± 0.03 × 6.09 ± 0.05 × 10.01 ± 0.09 mm (Fig. 1A–C), and the actual porosity was 55.1 ± 0.8%. According to the SEM observation and quantitative measurement, the exact pore dimension (536.3 ± 2.1 µm; Fig. 1E) was slightly smaller than the designed value. Owing to the inhomogeneous linear shrinkage along the z-axis direction during the sintering process, the circular pores showed an elliptical morphology in the side view. In addition, typical silicate crystal structures were observed on the surfaces of the nCSi scaffolds at progressively increasing magnifications of the SEM micrographs (Fig. 1F).

3.3. Biodissolution of scaffolds in vitro

The in vitro degradation behavior was analyzed by maintaining the
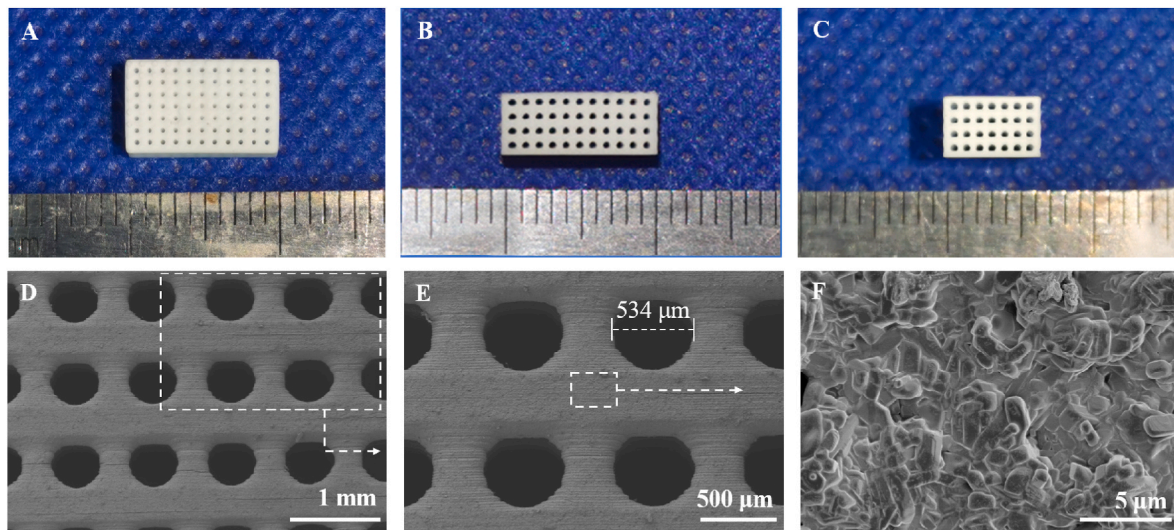
Fig. 1. (A) Planform of the sintered scaffold (B) Front view of the scaffold (C) Left view of the scaffold (D–F) SEM images ($\times 30$, $\times 50$) of the microstructures of representative scaffolds (n = 3) (F) Magnified structure of nCSi ceramic phases on the strut surface ($\times 6000$). The white dotted lines and arrows indicate the magnified structures of the located areas.

sintered scaffolds in Tris buffer for 2, 4, and 6 weeks. The remaining masses of the samples are shown in Fig. 2A. After 6 weeks, $92.8 \pm 1.4\%$ of the nCSi scaffold mass remained. During immersion, the strength of the bioceramic scaffolds decreased (Fig. 2B). nCSi scaffolds showed an initial compressive strength of 37.2 ± 2.57 MPa. Strength was markedly reduced within the first 4 weeks. Then, a steady decrease of compressive strength appeared in the next 2 weeks and maintained approximately 18.13 ± 4.88 MPa after 6 weeks.

The ion release from the scaffolds during immersion was revealed by ICP analysis (Fig. 2C–F). It was observed that the Ca, Mg, and Si concentrations increased in the Tris buffer in accordance with the chemical composition of the bioceramic. In particular, the Ca and Mg concentrations gradually increased during immersion. However, the Si concentrations showed a rapid increase during days 0–7, a slow increase during days 7–14, and then remained stable for days 17–21. Meanwhile, the ion concentrations of Na were also subtly increased in the whole-time stage because a small amount of Na^+ from $Na_2SiO_3 \cdot 9H_2O$ can coprecipitate into nCSi powder during the synthesis.

### 3.4. Remineralization capacity of bioceramic scaffolds

The scaffolds were immersed in SBF for 1 or 2 weeks and observed using SEM. The porous structures were maintained (Fig. 3A and D), and a few granular precipitates were deposited on the scaffold after 1 week (Fig. 3B). After 2 weeks, the surface of the scaffolds was entirely covered by granule-like apatite mineral crystals (Fig. 3E). Quantitative EDS analysis revealed that less apatite was deposited on the surface of scaffolds after one week and showed a high Ca/P ratio (6.67) (Fig. 3C). As more hydroxyapatite formed and the apatite layer became thicker, the Ca/P reduced to 1.04 after 2 weeks (Fig. 3F).

3.5. General conditions and weight of experimental animals

A decrease in diet was observed in a few rabbits from both groups within two days, which may be attributable to postoperative pain. However, the movement, mental status, feces, urine, and other general conditions of the animals were normal. The operation area was slightly edematous in 1 week, and the wound healed completely after 1 week. No
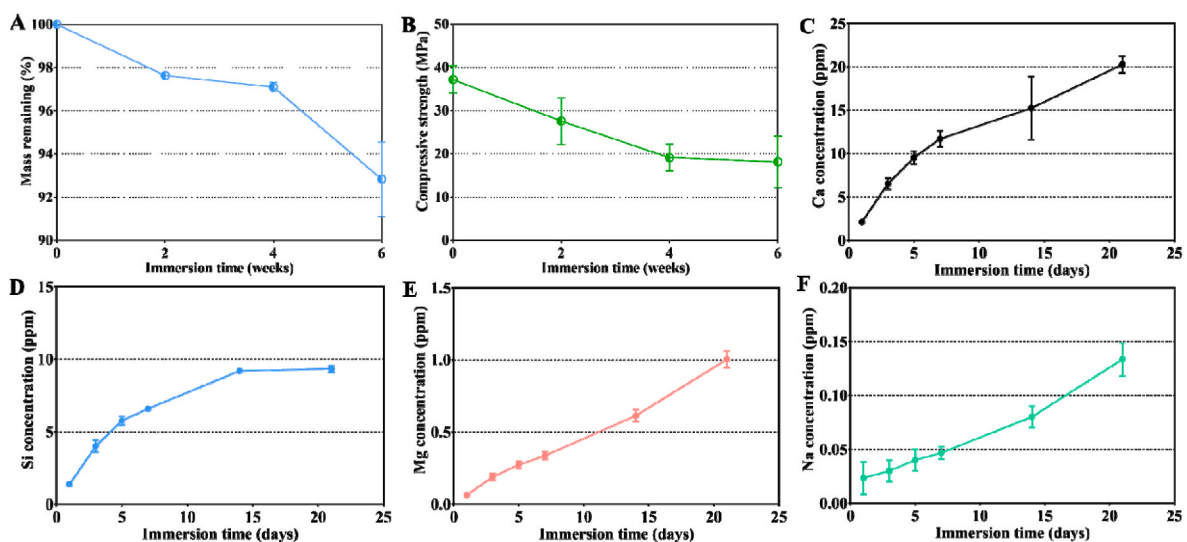
Fig. 2. Changes in mass (A) and compressive strength (B) of the bioceramic scaffolds after immersion in Tris buffers for 0–6 weeks (n = 3). Changes in the release of Ca (C), Si (D), Mg (E), and Na (F) ions in Tris buffer during the immersion test (results plotted as mean $\pm$ SD, n = 3).
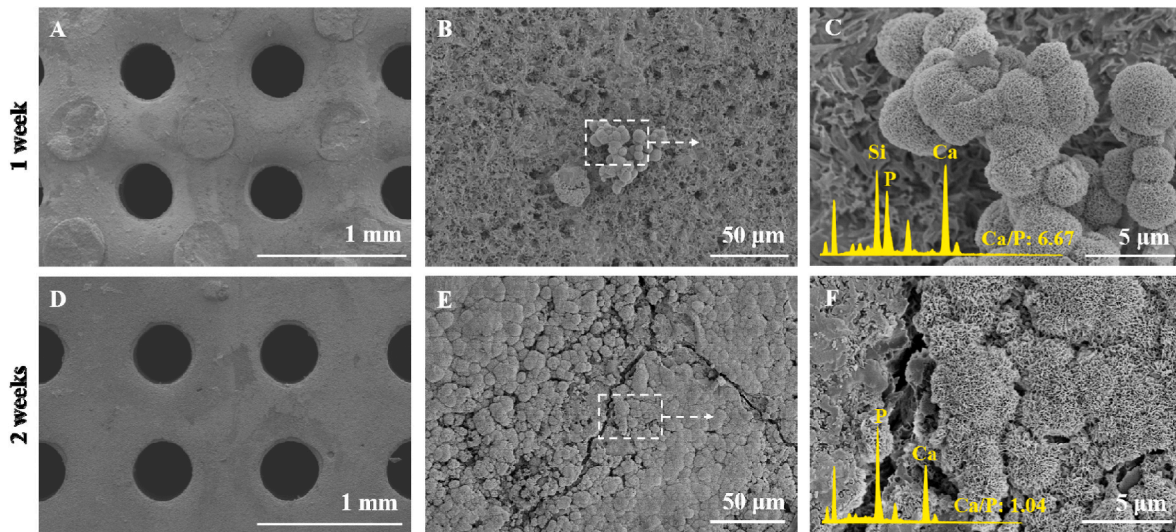
Fig. 3. SEM observation of the surface morphology of the bioceramic scaffolds and selected-area EDX spectra after immersion in SBF for two weeks (A, D) Surface of the bioceramic scaffolds (50 ×), (B, E) magnified surface morphology of the bioceramic scaffolds (1100 ×), and the white dotted line and arrows indicate the magnified structure of the located areas. The insets in (C, F) show face-scanning selected-area EDX spectra of the scaffold surface (6000 × magnification).

swelling, bleeding, or infection was subsequently observed in the surgical region. In addition, the weights of the animals increased normally, and no significant differences were observed between the two groups ($P > 0.05$, Figure S2; SI).

3.6. Haematological examination

No significant differences were found in the leukocyte-related indicators, except for NEUT and EO (Fig. 4B–H). NEUT and EO levels in the blank group increased at 3 days postoperatively and were significantly higher than those in the nCSi group. No inflammatory response
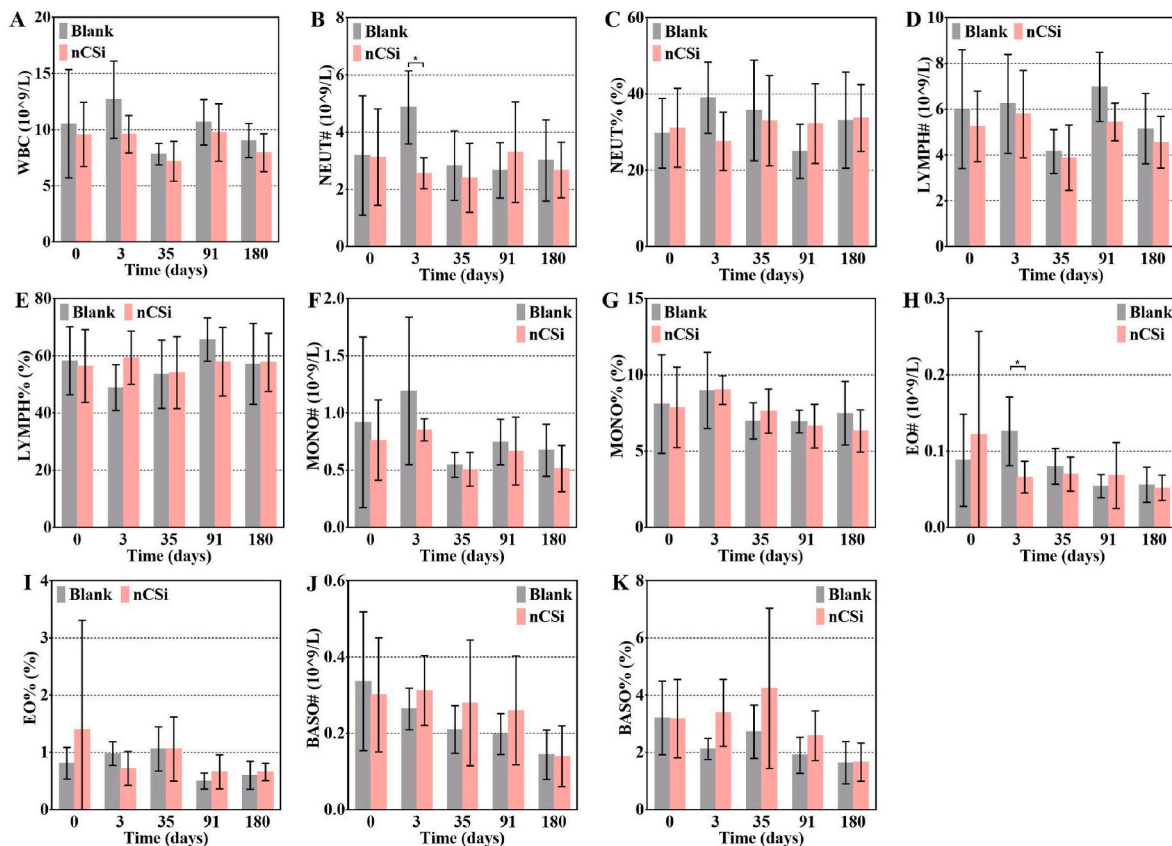
Fig. 4. Leukocyte-related indicators in haematological examinations (A) White blood cell (WBC), (B) neutrophil (NEUT), (C) neutrophil percentage (NEUT%), (D) lymphocyte (LYMPH), (E) lymphocyte percentage (LYMPH%), (F) monocyte (MONO), (G) monocyte percentage (MONO%), (H) eosinophils (EO), (I) eosinophils percentage (EO%), (J) basophilic granulocyte (BASO), (K) basophilic granulocyte percentage (BASO%). Results are plotted as mean ± SD, *$P < 0.05$, n = 20 at 0 days, n = 5 at 3–180 days, using Student's t-test.

was observed in the experimental group after the nCSi scaffold implantation. A lack of implants may lead to increased postoperative bleeding and cause a more serious inflammatory reaction. Fortunately, these differences disappeared 35 days postoperatively.

No significant differences in red blood cell parameters were observed between the blank and nCSi groups at any time point after the operation (Figure S3A–G; SI). Furthermore, no significant differences in platelet (Figure S3H–L; SI) or reticulocyte parameters (Figure S3M–O; SI) were observed between the two groups. The above results demonstrate that nCSi bioceramic scaffold implantation did not significantly affect the hematological indices of the animals.

3.7. Biochemical examination

The ALP (Fig. 5E), CR (Fig. 5F), CK (Fig. 5K), and K$^+$ (Fig. 5M) levels in the nCSi group were significantly lower than those in the blank group 3 days postoperatively. The nCSi group also exhibits a lower K$^+$ value at 180 d. The change in serum ALP levels is closely related to bone metabolism in the defect area [25]. Both groups showed significantly higher CK values 3 days after the operation. In addition, the serum CK level of the nCSi group was lower than that of the blank group, implying that the muscle injury during the operation and postoperative muscle fatigue in the nCSi group were weaker compared with the blank group [26,27]. Though the K$^+$ level of the experimental group was significantly lower than that of the blank group at 3 and 180 days after surgery, no statistical difference in K$^+$ level was found between the baseline (4.50 ± 0.37 mmol/L) and the K$^+$ level at 3 (4.54 ± 0.34 mmol/L) or 180 (4.38 ± 0.35 mmol/L) days. This suggests that the statistical differences in K$^+$ may be attributed to normal physiological fluctuations. Moreover, the reduction in the CR was generally not clinically significant.

3.8. Pathological analysis of the main apparatus

Three to 180 days after surgery, no significant abnormalities were observed in the color or texture of the main organs, including the heart,

liver, spleen, lung, kidney, and brain. As shown in Figure S4 (SI), no significant differences were observed in the wet weights of the main organs between the nCSi and blank groups ($P > 0.05$). Further histopathological observations of the major organs were performed.

Histological examination of the heart tissue revealed that the structure of the heart was clear in the experimental and blank groups. As shown in Fig. 6A, the cardiomyocytes were neatly arranged without obvious hemorrhage, edema, or inflammatory cell infiltration. Histological observations of the livers showed that the structure of the hepatic lobule was clear, and the structure of the portal area was normal in both groups. As shown in Fig. 6B, hepatocytes were arranged in the cords without significant hemorrhage, edema, or inflammatory cells.

Histological observations revealed that the structure of the spleens in each group was clear, with a normal structure of the splenic trabeculae. The central artery and germinal center are shown in Fig. 6C. Histological observation of the lungs showed that the structure of the lung tissue in each group was clear, and tracheal mucosal epithelial cells were arranged neatly. The alveolar structure was normal, and no notable hemorrhage or inflammatory cells were observed in the interstitium (Fig. 6D). The renal structure comprising the renal cortex and medulla was clear in the nCSi and blank groups. In the renal cortex, a large number of glomeruli with normal morphology were observed, and the renal tubules were neatly arranged. In addition, no hemorrhage, edema, or inflammatory cells were observed in the kidney interstitium, as shown in Figure S5(SI). Histological examinations of the cerebral cortexes, thymi, testes, epididymides, and adrenal glands were also performed, but no notable pathological changes were detected (Figure S6–10; SI). Overall, the implantation of the nCSi bioceramic scaffolds had no significant effect on the main organs of the experimental animals.

3.9. μCT reconstruction analysis

According to the μCT analyses (Fig. 7), only debris of bone tissue could be observed in the bone defects in the blank group at 3 days, but
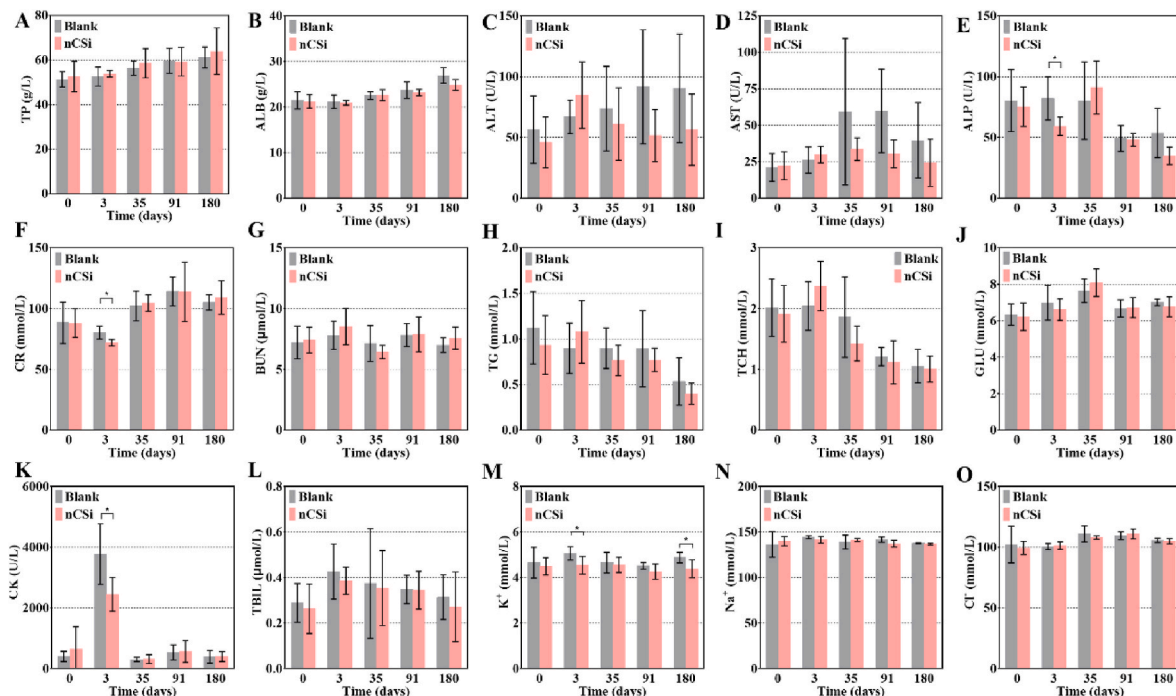
Fig. 5. Serum biochemical indicators 3, 35, 91, and 180 days after surgery (A) total protein (TP), (B) albumin (ALB), (C) alanine transaminase (ALT), (D) aspartate aminotransferase (AST), (E) alkaline phosphatase (ALP), (F) creatinine (CR), (G) blood urea nitrogen (BUN), (H) triglyceride (TG), (I) total cholesterol (TCH), (J) glucose (GLU), (K) creatine kinase (CK), (L) total bilirubin (TBIL), (M) potassium (K$^+$), (N) sodium (Na$^+$), (O) chlorine (Cl$^-$). Results are plotted as mean ± SD, *$P < 0.05$, n = 20 at 0 days, n = 5 at 3–180 days, using Student's t-test.
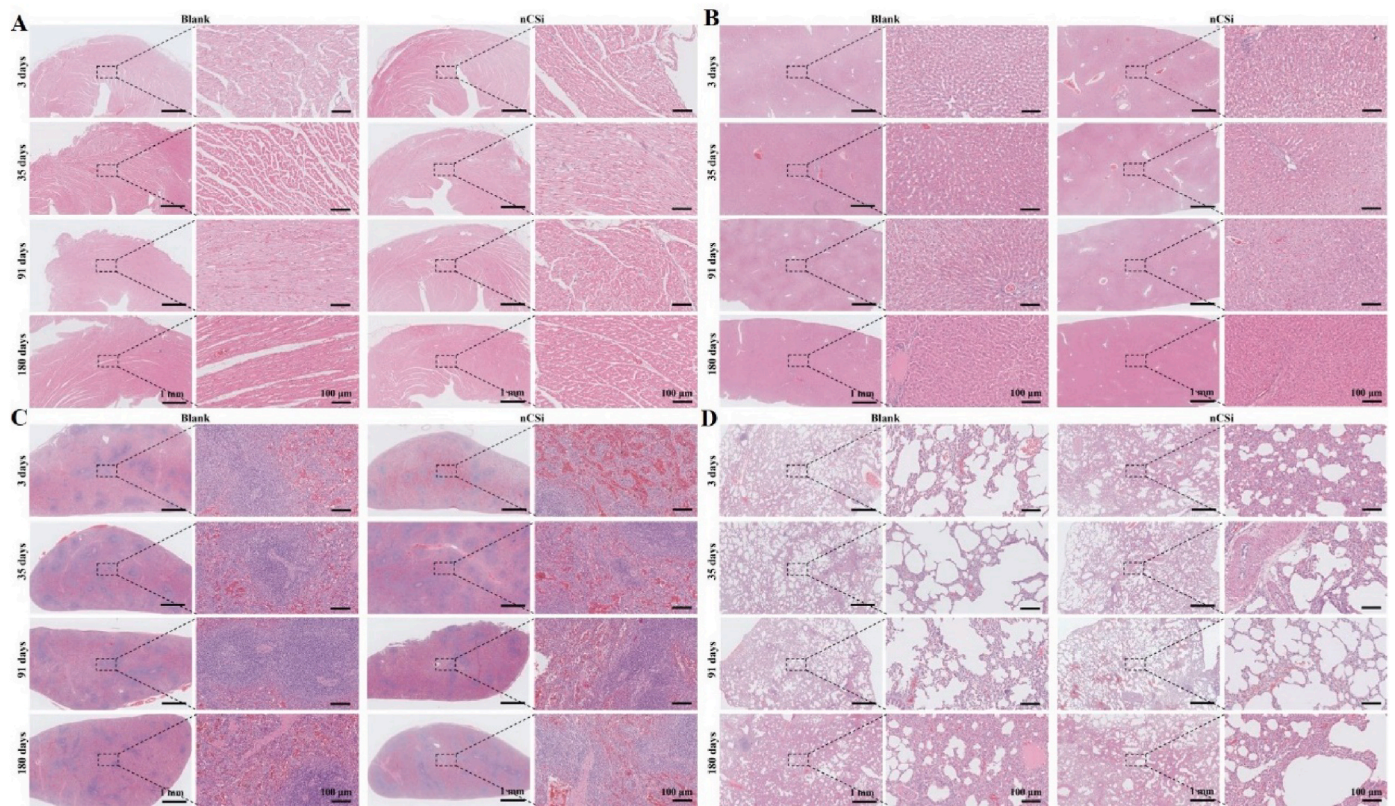
Fig. 6. Histopathological observations (× 20, × 200) of the major organs, including the (A) heart, (B) liver, (C) spleen, and (D) lung (n = 5, HE staining). The dotted boxes and dotted lines indicate the microstructures at high magnification.

the defect cavity in the nCSi group was occupied by distinct structures of the scaffold to restore the initial integrity of bone morphology and structure. The horizontal and coronal views inside the defect confirmed that the pores of the scaffolds were nearly entirely interconnected (Fig. 7b, c). After 35 days, although a large variety of new bone tissue ingrowth into the defects of the blank group (Fig. 7E–G), a notable depression (Fig. 7F and G, white arrows) was found in the defect area. Bioceramic scaffolds play an important role in maintaining the shape of the mandible with little bone tissue ingrowth into the macropores of the scaffolds. When implantation was extended to 91 days, more new bone tissue was formed within the defect of the blank group, but a depression on the surface of the bone persisted. In the nCSi group, the scaffolds were partially biodegraded and replaced with newly formed bone tissue, and bone morphology was relatively intact. At 180 days post-implantation, bone tissue reconstruction was completed in the blank group, and a marrow cavity was formed. However, bone depression was still observed in the defective zone. In the nCSi group, the bioceramic scaffolds were almost completely degraded and replaced by bone tissue to fill the bone defects.

The quantitative analyses of BV/TV, Tb.N, RV/TV, and Tb.Sp were consistent with the 2D/3D reconstruction observations (Fig. 7Q-T). No bone tissue could be observed in the defect in two groups at 3 days, but $43.90 \pm 1.96\%$ volume of the defect in the nCSi group was occupied by the scaffold. Significantly higher BV/TV and Tb.N data in the blank group implied appreciable alveolar bone ingrowth at 35 days post-operatively. The scaffolds were partially biodegraded with little bone tissue ingrowth in the nCSi group. After 91 days, the BV/TV and Tb.N in the blank group was decreased. Although the bioceramic scaffolds were further degraded and replaced by newly formed bone tissue, the BV/TV and Tb.N was lower than that of the blank group. At 180 days post-implantation, the bone tissue in the blank group continued to decline. In addition, the bioceramic scaffolds showed full biodegradation in the nCSi group, with higher BV/TV and Tb.N values ($P < 0.05$). In addition,

Tb.Sp in the blank group was lower than that in the nCSi group on day 3 and gradually increased, accompanied by a decrease in Tb.N. However, the value of Tb.Sp in the nCSi group showed the opposite trend from day 35–180.

The above results demonstrate that appreciable alveolar bone ingrowth appeared in the early stages of wound healing in the blank group, but bone reconstruction and resorption also occurred rapidly. However, the newly formed bone tissue grew into the defect region of the nCSi group with degradation of the bioceramic scaffolds and increased and exceeded that of the blank group.

3.10. Histological analysis

Histological staining was conducted to explore bone tissue healing in the bone defects. Fig. 8A and E shows only blood exudation and tissue debris in the defects of the blank group, whereas the defect in the nCSi group was occupied by the scaffold after 3 days. At 35 days, a large amount of bone tissue had grown into defects in the blank group. However, no bone filling was observed in the central area of the defect. In the nCSi group, the defects were effectively filled with bioceramic scaffolds, and new bone tissue grew in the porous networks of the bioceramic scaffolds. At 91 days, although appreciable new bone tissue was observed in the defect in the blank group (Fig. 8C–G), no bone tissue repair was observed in some defect areas. In the nCSi group, the bioceramic scaffold gradually degraded, and new bone tissue grew into the defect and bound tightly to the surface of the scaffold. At 180 days post implantation, bone remodeling was nearly complete, as mature bone marrow was observed in the defect. In the nCSi group, the bioceramic scaffold was generally degraded and successfully replaced with the woven bone tissue, and only a few residual biomaterials were observed.

MacNeal's trichrome staining was consistent with HE staining. In the blank group, new bone tissue grew rapidly in the early stage and gradually remodeled and decreased. After 35 and 91 days, connective tissue
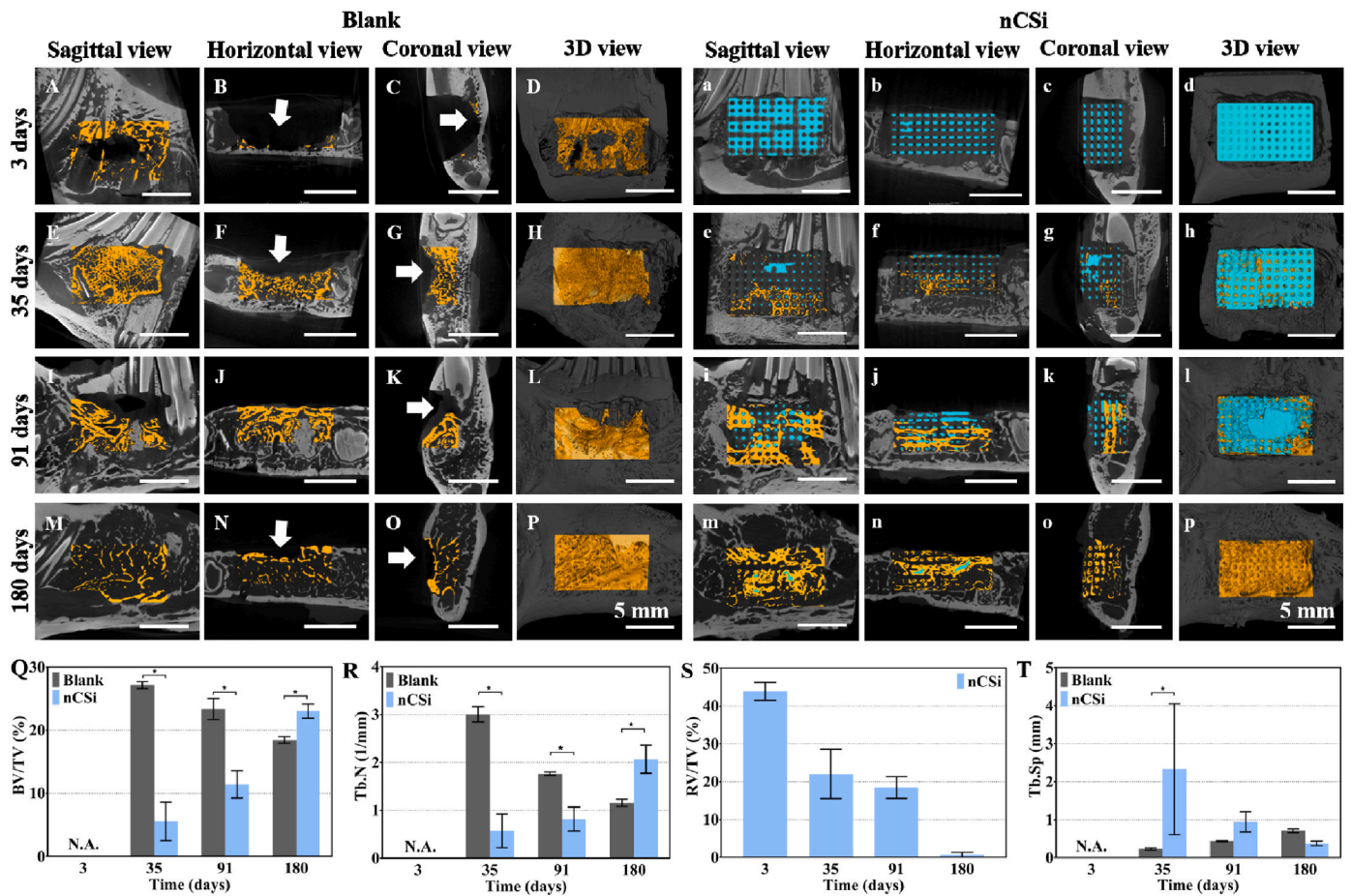
Fig. 7. 2D/3D μCT reconstructed images of the defects in blank (A–P) and nCSi (a–p) groups at 3–180 days postoperatively (White arrows indicating the hollows of the defects. Yellow, new bone; blue, residual material) (Q–T) Quantitative data on newly formed bone volume/total volume (BV/TV) ratio and trabecular number (Tb.N), residual scaffold volume/total volume (RV/TV), trabecular separation (Tb.Sp) based on μCT (results are plotted as mean ± SD, *$P < 0.05$, n = 3, using Student's t-test). (For interpretation of the references to color in this figure legend, the reader is referred to the Web version of this article.)
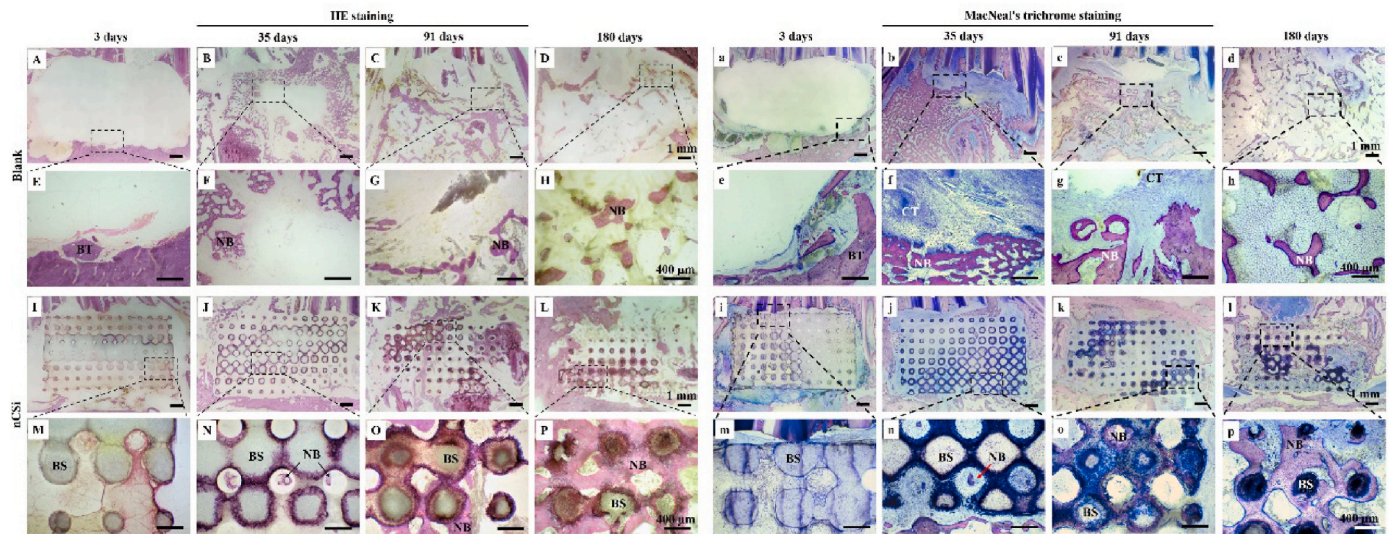
Fig. 8. (A–P) HE and (a–p) MacNeal's trichrome staining ($\times 10$, $\times 40$) of new bone formation in defects at 3–180 days postoperatively (n = 3). The dotted boxes and dotted lines indicate the microstructures at high magnification. NB, newly formed bone; BS, bioceramic scaffold; CT, connective tissue; BT, bone tissue.

ingrowth was observed in the defective area (Fig. 8f and g). A medullary cavity appears in the central part of the defect after 180 days. nCSi scaffolds play an important role in maintaining the shape and contour of the mandible. Although only a small amount of mature tissue can grow into a defect during the early stages of healing, porous architectures can be biodegraded over time, accompanied by gradual new bone ingrowth.

New bone tissue gradually increased in the defect group and was significantly greater than that in the blank group at 180 days. In addition, the bioceramic scaffolds showed good osseointegration ability, and no traces of immune–inflammatory reactions were found between the surrounding tissue and the surface of the scaffolds.

4. Discussion

Porous bioceramic scaffolds with 55% porosity were manufactured using DLP-based 3D printing. The nCSi scaffolds showed a compressive strength of 37.2 ± 2.57 MPa, which was much higher than 2–6 MPa of cancellous bone [28] and can maintain the regeneration space in the alveolar defects. The porous scaffolds also exhibited an appreciable apatite-forming ability after immersion in SBF. After 2 weeks of immersion, hydroxyapatite was formed on the surface of the scaffold with a Ca/P ratio of 1.04. The apatite-depositing ability on the surface of biomaterials is the key to achieving osseointegration between the material and living bone after implantation [29]. During the in vitro immersion experiment, a large number of Ca and Si ions and a small number of Mg ions released from the scaffolds provided an ideal environment for osteogenic differentiation. Xu [19] cocultured bone marrow-derived mesenchymal stem cells (BMSCs) from Sprague–Dawley rats with CSi–Mg6 scaffolds (containing 16% CSi). After 7 days of coculture, the relative expression of osteogenic marker genes, including COL-1, osteocalcin (OCN), osteopontin (OPN), and bone morphogenetic protein (BMP-2), was significantly higher than that in the control group. In addition, in vitro studies by Fiocco et al. [30] found that the incorporation of Mg into CSi plays a significant role in the enhancement of osteogenic differentiation and matrix formation in pre-osteoblast cells.

The biocompatibility of the nCSi scaffold was evaluated in vivo after verifying its excellent mechanical strength and bioactivity. Although some studies have shown that CSi and nCSi display good cytocompatibility [31–33], only a few have evaluated the potential systemic toxicity of CSi ceramics or their composites. In 2019, Paraš [34] filled polyethylene tubes with Ca-silicate cement and implanted tubes in a subcutaneous pocket of rats. According to the stereological and histological measurements of the liver, although the volume density of hepatocytes and sinusoids showed significant differences between the control and experimental animals, these changes in the liver tissue were not pathological. This conclusion was supported by the analysis of hematological parameters, which were not significantly different between the control and experimental groups. Other researchers [22] prepared polyetheretherketone (PEEK)/CSi composite/porous tantalum interbody fusion cages and implanted them in the C2/C3 and C3/C4 intervertebral spaces in goats. ICP data showed that abnormal systemic metabolism or accumulation of calcium and silicon did not occur in local tissues or major organs after CS/PEEK cage implantation. Moreover, no notable pathological changes were observed in the heart, liver, spleen, or kidneys. Similarly, in this study, the body weight and histopathology of the main organs of the animals did not reveal any significant differences between the nCSi and blank groups. Thus, it is reasonable to assume that nCSi possesses credible biosafety and has the potential for application in clinical translation.

Blood analysis revealed no significant differences in hematological parameters between the nCSi and blank groups, except for NEUT and EO, which were lower in the nCSi group on day 3. These results indicated that in vivo implantation of nCSi resulted in no myelotoxic or autoimmune effects on peripheral blood cells. Implantation reduced the acute inflammatory response postoperatively. Furthermore, the biochemical analysis revealed that the serum ALP level in the experimental group was significantly lower than that in the blank group at 3 days ($P < 0.05$). ALP has been used as a common index for the evaluation of diseases of the hepatobiliary system and bone tissue [35]. Serum ALP levels may change during bone tissue repair and remodeling. Balbinot [36] produced niobium-containing bioactive glass scaffolds and surgically implanted them in the femur of rats, and ALP activity was

quantified following the collection of blood serum samples. Fifteen days after surgical implantation, ALP levels increased in all groups. After early-stage repair, the maturation of new bone leads to a reduction in serum ALP activity. Ahmadipour [37] injected a calcitonin-enriched hydrogel scaffold into the defect of the rat femur, and then the serum ALP concentration was measured by biochemical analysis. ALP levels in the defect-induced groups were higher than those in the control group without defects ($P < 0.05$) on 1 day, but no differences were observed among the former groups. Muljačić [38] believes that ALP activity may serve as a marker of the stability of fracture and the rate of bone healing after measuring the activity of ALP of 41 patients who had sustained long bone fractures. It can be concluded that a minor increase or no change in ALP activity in the first two weeks indicates successful fracture fixation and rapid bone healing. By contrast, a significant increase in ALP levels indicates deficient fracture fixation and delayed bone repair. Bearing this in mind, it is reasonable to assume that the reduction in ALP levels in the nCSi group 3 days after surgery might be attributed to the improved initial stability of defects by nCSi scaffold implantation.

Finally, the alveolar bone regeneration potential of the nCSi bioceramics was evaluated using a rabbit alveolar bone defect model. According to micro-CT and histological analyses, a large number of new bone tissues were formed in the blank group at 35 days, but a notable depression was found in the defect area. With an increase in observation time, the volume of bone in the defect gradually decreased and was replaced by the bone marrow cavity. Cardaropoli [39] performed histological morphometric measurements to study the bone tissue formation and remodeling of an extraction socket. From days 14–30, the percentage of mineralized bone in the socket increased from 48 ± 29.4% to 88 ± 8.7%. However, bone marrow replaced the mineralized bone tissue during the healing process, which decreased to 15 ± 11.1% on day 180. Covani [40] also evaluated alveolar bone remodeling after tooth extraction in rabbit incisor sockets. Micro-CT analysis revealed a bone volume loss of 41% from baseline to day 14, which increased to 58.1% by day 90. Thus, although newly formed bone can rapidly occupy the alveolar defect volume without biomaterial implantation, avoiding distinct bone remodeling and dimensional resorption remains challenging. Furthermore, nCSi scaffolds played an important role in maintaining the dimensions of the alveoli and avoiding collapse of the bone, and the newly formed bone gradually grew into a defect with the degradation of the scaffolds. Although bone formation was slow in the early stages, the volume of new bone in the defect exceeded that in the blank group at 180 days. Machtei [41] compared the dimensional changes and bone quality of biphasic calcium sulfate/hydroxyapatite (BCS/HA), bovine-derived xenografts (BDX), and no grafting (control) for socket preservation. Four months postoperatively, both the BCS/HA and BDX groups demonstrated less vertical and horizontal bone loss than the nongrafted control group. Conversely, the percentage of bone in the control group was substantially greater than those in the BCS/HA and BDX groups. Recently, a similar phenomenon was observed by Canellas [42]. In a network meta-analysis of 38 randomized clinical trials conducted from 2003 to 2019, no available grafting biomaterial was found to improve the percentage of new bone formation between 3 and 6 months. Biomaterials with slow biodegradation characteristics may be more useful for maintaining alveolar dimensions after tooth extraction.

To the best of our knowledge, this is the first study to investigate the systemic toxicity of nonstoichiometric wollastonite scaffolds. Although the current study was not performed in compliance with Good Laboratory Practice (GLP) principles, various measurements, including general condition monitoring, hematological examination, biochemical examination, and pathological analysis, were performed to evaluate the biocompatibility and osteogenic capability of the nCSi scaffolds. Additionally, the subacute, subchronic, and chronic systemic toxicity of the nCSi scaffolds was partly reflected in this long experimental period, lasting for nearly half a year. The main limitation of this study is its small sample size. For clinical translation, the genotoxicity, neurotoxicity, immunotoxicity, and reproductive and developmental toxicity of nCSi

scaffolds also need to be studied further.

5. Conclusions

This study systematically investigated the biocompatibility and osteogenic properties of porous bioceramic scaffolds fabricated using a DLP-based 3D printing method. In vitro experiments revealed that the nCSi scaffolds exhibited desirable physicochemical properties and biological performance. The rabbit alveolar defect model confirmed that such bioceramic scaffolds had no significant effect on the hematological indices, biochemical indices, or main organs of the experimental animals. The scaffolds exhibited slow bone formation efficacy in the early stage but finally exceeded that of the control group at 180 days. Porous scaffolds are important in maintaining alveolar dimensions and avoiding bone collapse. These new findings are promising for designing optimal nCSi scaffolds for alveolar bone repair and clinical translation in the near future.

Author contributions

Yingming Wei and Zhongxiu Wang: materials preparation, sample testing, statistics collection and analyzing, article writing; Yingming Wei, Jiayin Han and Shuaiqi Zhong: in vivo trials and specimen collection; Lihong Lei: proofread the paper; Xianyan Yang: μCT guidance and technical guidance; Lili Chen and Zhongru Gou: financial support, experimental proposal and writing guidance.

Declaration of competing interest

The authors have no conflicts of interest relevant to this article.

Acknowledgements

Appendix A. Supplementary data

Supplementary data to this article can be found online at https://doi.org/10.1016/j.jot.2024.02.004.

References

[1] Wei Y, Wang Z, Han J, Jiang X, Lei L, Yang X, et al. Modularized bioceramic scaffold/hydrogel membrane hierarchical architecture beneficial for periodontal tissue regeneration in dogs. Biomater Res 2022;26:68.

[2] Gibon E, Lu LY, Nathan K, Goodman SB. Inflammation, ageing, and bone regeneration. J Orthop Translat 2017;10:28–35.

[3] Beube FE. A study on reattachment of the supporting structures of the teeth. J Periodontol 1947;18(2):55–66.

[4] Deng C, Chang J, Wu C. Bioactive scaffolds for osteochondral regeneration. J Orthop Translat 2019;17:15–25.

[5] Wang X, Ye M, Shen J, Li J, Li Y, Bao Z, et al. Core-shell-typed selective-area ion doping wollastonite bioceramic fibers enhancing bone regeneration and repair in situ. Appl Mater Today 2023;32:101849.

[6] Li H, Xue K, Kong N, Liu K, Chang J. Silicate bioceramics enhanced vascularization and osteogenesis through stimulating interactions between endothelia cells and bone marrow stromal cells. Biomaterials 2014;35:3803–18.

[7] Liu A, Sun M, Shao HF, Yang XY, Ma CY, He DS, et al. The outstanding mechanical response and bone regeneration capacity of robocast dilute magnesium-doped wollastonite scaffolds in critical size bone defects. J Mater Chem B 2016;4:3945–58.

[8] Xu S, Lin K, Wang Z, Chang J, Wang L, Lu J, et al. Reconstruction of calvarial defect of rabbits using porous calcium silicate bioactive ceramics. Biomaterials 2008;29:2588–96.

[9] Liu X, Zhao N, Liang H, Tan B, Huang F, Hu H, et al. Bone tissue engineering scaffolds with HUVECs/hBMSCs cocultured on 3D-printed composite bioactive ceramic scaffolds promoted osteogenesis/angiogenesis. J Orthop Translat 2022;37:152–62.

[10] Yue X, Zhao L, Yang J, Jiao X, Wu F, Zhang Y, et al. Comparison of osteogenic capability of 3D-printed bioceramic scaffolds and granules with different porosities for clinical translation. Front Bioeng Biotechnol 2023;11:1260639.

[11] Wang G, Lu Z, Dwarte D, Zreiqat H. Porous scaffolds with tailored reactivity modulate in-vitro osteoblast responses. Mater Sci Eng C 2012;32:1818–26.

[12] Ni S, Chang J. In vitro degradation, bioactivity, and cytocompatibility of calcium silicate, dimagnesium silicate, and tricalcium phosphate bioceramics. J Biomater Appl 2009;24:139–58.

[13] Shirazi FS, Moghaddam E, Mehrali M, Oshkour AA, Metselaar HS, Kadri NA, et al. In vitro characterization and mechanical properties of beta-calcium silicate/POC composite as a bone fixation device. J Biomed Mater Res 2014;102:3973–85.

[14] Shirazi FS, Mehrali M, Oshkour AA, Metselaar HS, Kadri NA, Abu Osman NA. Mechanical and physical properties of calcium silicate/alumina composite for biomedical engineering applications. J Mech Behav Biomed Mater 2014;30:168–75.

[15] Xie J, Yang X, Shao H, Ye J, He Y, Fu J, et al. Simultaneous mechanical property and biodegradation improvement of wollastonite bioceramic through magnesium dilute doping. J Mech Behav Biomed Mater 2016;54:60–71.

[16] Li Y, Wu R, Yu L, Shen M, Ding X, Lu F, et al. Rational design of nonstoichiometric bioceramic scaffolds via digital light processing: tuning chemical composition and pore geometry evaluation. J Biol Eng 2021;15:1.

[17] Shao H, Sun M, Zhang F, Liu A, He Y, Fu J, et al. Custom repair of mandibular bone defects with 3D printed bioceramic scaffolds. J Dent Res 2018;97:68–76.

[18] Qin H, Wei Y, Han J, Jiang X, Yang X, Wu Y, et al. 3D printed bioceramic scaffolds: adjusting pore dimension is beneficial for mandibular bone defects repair. J Tissue Eng Regen Med 2022;16:409–21.

[19] Xu C, Wu F, Yang J, Wang H, Jiang J, Bao Z, et al. 3D printed long-term structurally stable bioceramic dome scaffolds with controllable biodegradation favorable for guided bone regeneration. Chem Eng J 2022;450:138003.

[20] Wang J, Dai X, Peng Y, Liu M, Ye J. Digital light processing strength-strong ultra-thin bioceramic scaffolds for challengeable orbital bone regeneration and repair in Situ. Appl Mater Today 2021;22:100889.

[21] Lei L, Wei Y, Wang Z, Han J, Sun J, Chen Y, et al. Core-Shell bioactive ceramic robocasting: tuning component distribution beneficial for highly efficient alveolar bone regeneration and repair. ACS Biomater Sci Eng 2020;6:2376–87.

[22] Yuan K, Zhang K, Yang Y, Lin Y, Zhou F, Mei J, et al. Evaluation of interbody fusion efficacy and biocompatibility of a polyetheretherketone/calcium silicate/porous tantalum cage in a goat model. J Orthop Translat 2022;36:109–19.

[23] Hewitt CD, Innes DJ, Savory J, Wills MR. Normal biochemical and hematological values in New Zealand white rabbits. Clin Chem 1989;35:1777–9.

[24] Javed H, Shah SNH, Iqbal FM, Javed N, Saeed B. A hematological and histopathological study on diphenhydramine nasal nano-gel and nano-emulgel for the management of allergic rhinitis in animal model. AAPS PharmSciTech 2023;24:55.

[25] Stoffel K, Engler H, Kuster M, Riesen W. Changes in biochemical markers after lower limb fractures. Clin Chem 2007;53:131–4.

[26] Ten Haaf DSM, Bongers C, Hulshof HG, Eijsvogels TMH, Hopman MTE. The impact of protein supplementation on exercise-induced muscle damage, soreness and fatigue following prolonged walking exercise in vital older adults: a randomized double-blind placebo-controlled trial. Nutrients 2020;12.

[27] Cialoni D, Brizzolari A, Sponsiello N, Lancellotti V, Lori C, Bosco G, et al. Serum cardiac and skeletal muscle marker changes in repetitive breath-hold diving. Sports Med Open 2021;7:58.

[28] Subramaniam S, Fang YH, Sivasubramanian S, Lin FH, Lin CP. Hydroxyapatite-calcium sulfate-hyaluronic acid composite encapsulated with collagenase as bone substitute for alveolar bone regeneration. Biomaterials 2016;74:99–108.

[29] Li Y, Li J, Jiang S, Zhong C, Zhao C, Jiao Y, et al. The design of strut/TPMS-based pore geometries in bioceramic scaffolds guiding osteogenesis and angiogenesis in bone regeneration. Mater Today Bio 2023;20:100667.

[30] Fiocco L, Li S, Stevens MM, Bernardo E, Jones JR. Biocompatibility and bioactivity of porous polymer-derived Ca-Mg silicate ceramics. Acta Biomater 2017;50:56–67.

[31] Lin YH, Lee AK, Ho CC, Fang MJ, Kuo TY, Shie MY. The effects of a 3D-printed magnesium-/strontium-doped calcium silicate scaffold on regulation of bone regeneration via dual-stimulation of the AKT and WNT signaling pathways. Biomater Adv 2022;133:112660.

[32] Tsamesidis I, Gkiliopoulos D, Pouroutzidou GK, Lymperaki E, Papoulia C, Reybier K, et al. Effect of artemisinin-loaded mesoporous cerium-doped calcium silicate nanopowder on cell proliferation of human periodontal ligament fibroblasts. Nanomaterials 2021;11.

[33] Lai WY, Chen YJ, Lee AK, Lin YH, Liu YW, Shie MY. Therapeutic effects of the addition of fibroblast growth factor-2 to biodegradable gelatin/magnesium-doped calcium silicate hybrid 3D-printed scaffold with enhanced osteogenic capabilities for critical bone defect restoration. Biomedicines 2021;9.

[34] Paras S, Jankovic O, Trisic D, Colovic B, Mitrovic-Ajtic O, Dekic R, et al. Influence of nanostructured calcium aluminate and calcium silicate on the liver: histological and unbiased stereological analysis. Int Endod J 2019;52:1162–72.

[35] Seo MS, Shim JY, Lee YJ. Relationship between serum alkaline phosphatase level, C-reactive protein and leukocyte counts in adults aged 60 years or older. Scand J Clin Lab Invest 2019;79:233–7.

[36] de Souza Balbinot G, Leitune VCB, da Cunha Bahlis EA, Ponzoni D, Visioli F, Collares FM. Niobium-containing bioactive glasses modulate alkaline phosphatase activity during bone repair. J Biomed Mater Res B Appl Biomater 2023;111:1224–31.

[37] Ahmadipour S, Varshosaz J, Hashemibeni B, Manshaei M, Safaeian L. In vivo assessment of bone repair by an injectable nanocomposite scaffold for local co-

delivery of autologous platelet-rich plasma and calcitonin in a rat model. Drug Dev Ind Pharm 2022;48:98–108.

[38] Muljacic A, Poljak-Guberina R, Zivkovic O, Bilic V, Guberina M, Crvenkovic D. Course and rate of post-fracture bone healing in correlation with bone-specific alkaline phosphatase and bone callus formation. Coll Antropol 2013;37:1275–83.

[39] Cardaropoli G, Araújo M, Lindhe J. Dynamics of bone tissue formation in tooth extraction sites. An experimental study in dogs. J Clin Periodontol 2003;30: 809–18.

[40] Covani U, Giammarinaro E. Alveolar bone remodeling with or without collagen filling of the extraction socket: a high-resolution X-ray tomography animal study 2022;11.

[41] Machtei EE, Mayer Y, Horwitz J, Zigdon-Giladi H. Prospective randomized controlled clinical trial to compare hard tissue changes following socket preservation using alloplasts, xenografts vs no grafting: clinical and histological findings. Clin Implant Dent Relat Res 2019;21:14–20.

[42] Canellas J, Ritto FG, Figueredo C, Fischer RG, de Oliveira GP, Thole AA, et al. Histomorphometric evaluation of different grafting materials used for alveolar ridge preservation: a systematic review and network meta-analysis. Int J Oral Maxillofac Surg 2020;49:797–810.